Ultrafast 25-fs relaxation in highly excited states of methyl azide mediated by strong nonadiabatic coupling

William K. Peters[a,b,1], David E. Couch[a,b], Benoit Mignolet[c], Xuetao Shi[d], Quynh L. Nguyen[a,b], Ryan C. Fortenberry[e], H. Bernhard Schlegel[d], Françoise Remacle[c], Henry C. Kapteyn[a,b], Margaret M. Murnane[a,b,1], and Wen Li[d]

[a]JILA, University of Colorado, Boulder, CO 80309; [b]Department of Physics, University of Colorado, Boulder, CO 80309; [c]Theoretical Physical Chemistry, Unité de Recherche Molecular Systems (UR MOLSYS) University of Liège, B4000 Liège, Belgium; [d]Department of Chemistry, Wayne State University, Detroit, MI 48202; and [e]Department of Chemistry and Biochemistry, Georgia Southern University, Statesboro, GA 30460

Contributed by Margaret M. Murnane, October 14, 2017 (sent for review July 16, 2017; reviewed by Elliot Bernstein and Arthur Suits)

Highly excited electronic states are challenging to explore experimentally and theoretically—due to the large density of states and the fact that small structural changes lead to large changes in electronic character with associated strong nonadiabatic dynamics. They can play a key role in astrophysical and ionospheric chemistry, as well as the detonation chemistry of high-energy density materials. Here, we implement ultrafast vacuum-UV (VUV)-driven electron–ion coincidence imaging spectroscopy to directly probe the reaction pathways of highly excited states of energetic molecules—in this case, methyl azide. Our data, combined with advanced theoretical simulations, show that photoexcitation of methyl azide by a 10-fs UV pulse at 8 eV drives fast structural changes and strong nonadiabatic coupling that leads to relaxation to other excited states on a surprisingly fast timescale of 25 fs. This ultrafast relaxation differs from dynamics occurring on lower excited states, where the timescale required for the wavepacket to reach a region of strong nonadiabatic coupling is typically much longer. Moreover, our theoretical calculations show that ultrafast relaxation of the wavepacket to a lower excited state occurs along one of the conical intersection seams before reaching the minimum energy conical intersection. These findings are important for understanding the unique strongly coupled non-Born–Oppenheimer molecular dynamics of VUV-excited energetic molecules. Although such observations have been predicted for many years, this study represents one of the few where such strongly coupled non-Born–Oppenheimer molecular dynamics of VUV-excited energetic molecules have been conclusively observed directly, making it possible to identify the ultrafast reaction pathways.

conical intersection | nonadiabatic dynamics | Rydberg–valence electronic states | PEPICO

Highly excited neutral electronic states present many challenges and opportunities for exploring strongly correlated nonadiabatic dynamics. A distinguishing aspect of highly excited neutral molecular systems, compared with the well-studied lower excited states, is that these electronic states are closely spaced and strongly coupled, even in the Franck–Condon region, enabling new and faster relaxation pathways. Molecular dynamics at large internal energies impact a variety of natural phenomena, from thermosphere–mesosphere coupling (1, 2) to astrochemical processes (3, 4). It has also been argued that excited states are critical in initiating explosions in high-energy materials (5–8). However, comparatively little work has been done on these systems since they can only be safely handled in small quantities, and, until recently, no sources were available that could produce several-electronvolt tunable light with femtosecond time resolution to directly probe these states experimentally. Furthermore, highly excited electronic potential energy surfaces are challenging to describe theoretically—due to the large density of states and the fact that small structural changes can lead to large changes in the electronic character of the states.

When molecules are excited by vacuum-UV (VUV) light in the 7- to 10-eV range, just below the ionization potential, one or several excited states can be accessed depending on the bandwidth of the pulse. In this energy range, there is typically a dense manifold of valence and Rydberg states that are often strongly coupled, each with an associated vibrational structure (9). As a result, VUV molecular absorption spectra typically contain quasicontinuous but structured bands with overlapping sharp peaks, indicating the wide variety of timescales and states involved. This differs from the lowest few excited states, where dynamics are dominated by only one or two electronic states. Depending on the character of the electronic state or the band of excited states accessed by the VUV pulse, different relaxation pathways, such as nonadiabatic relaxation, fluorescence, internal conversion, or dissociation on the excited state may occur. Consequently, small changes in photon energy can lead to dramatically different energetic pathways that are still incompletely understood and are a focus of intense current research.

These relaxation pathways also have completely different timescales. For instance, molecules excited by visible light can relax either by fluorescence on nanosecond timescales or through conical intersections, typically on femtosecond to picosecond timescales. The relaxation through conical intersections—molecular

Significance

Highly excited states of neutral molecules behave qualitatively differently than the lower excited states that are commonly studied in photochemistry. Such states are involved in ionospheric and astrochemical phenomena, as well as in detonation processes. However, highly excited states are poorly understood due to experimental and theoretical challenges in probing their complex dynamics. Here, we apply vacuum-UV femtosecond laser sources and an imaging photoelectron–photoion coincidence spectrometer to directly probe the surprisingly fast 25-fs reaction pathway of the energetic molecule methyl azide. Combined with advanced calculations, we conclude that the electronic relaxation is driven by strong nonadiabatic coupling and that population transfer occurs along a seam well above the minimum energy conical intersection.

Author contributions: W.K.P., D.E.C., B.M., R.C.F., H.B.S., F.R., H.C.K., M.M.M., and W.L. designed research; W.K.P., D.E.C., B.M., X.S., Q.L.N., R.C.F., H.B.S., and F.R. performed research; W.K.P., D.E.C., B.M., X.S., Q.L.N., R.C.F., H.B.S., F.R., H.C.K., M.M.M., and W.L. analyzed data; and W.K.P., B.M., and M.M.M. wrote the paper.

Reviewers: E.B., Colorado State University; and A.S., University of Missouri.

The authors declare no conflict of interest.

See Commentary on page 13594.

[1]To whom correspondence may be addressed. Email: william.peters@colorado.edu or Margaret.Murnane@colorado.edu.

This article contains supporting information online at www.pnas.org/lookup/suppl/doi:10.1073/pnas.1712566114/-/DCSupplemental.

geometries where two or more electronic states come into a degeneracy—are known to play a ubiquitous role in the dynamics of electronically excited states (10, 11). In polyatomic molecules, conical intersections exist along multidimensional "seams," and the population transfer can occur anywhere along the seam. The minimum energy along the seam is the minimum energy conical intersection (MECI) (12–14) and is the geometry usually reported in the literature. In the case of VUV excitation, it has long been known that a molecule will usually relax to its lowest excited state much faster than fluorescence (Kasha's rule) (15), which is currently understood to be a consequence of the increased density of states, which provides a richer landscape of potential conical intersections; indeed, highly excited molecules are speculated to relax through a sequence of successive conical intersections (16, 17). Such pathways are thought to play an important role in explosive molecules (5, 18).

For polyatomic molecules, the potential energy surfaces of the highly excited states that can be accessed by VUV pulses are typically different from those of the ground state. Therefore, the wavepacket experiences a force in the direction of the gradient, leading to fast structural changes in the first few femtoseconds after photon absorption. Along its way, the wavepacket can encounter a conical intersection seam (or a region of strong nonadiabatic coupling), where an efficient transfer of population to another electronic state can occur. The act of "passing through" a conical intersection involves a change in the electronic wavefunction, such that the vibrational wavepacket subsequently evolves on a different potential energy surface. The timescale for the nonadiabatic relaxation depends on coupling strength, the proximity of the strong nonadiabatic coupling region, and the topology of the conical intersection. If the conical intersection lies close to the Franck–Condon region and has a peaked topology (a pronounced funnel character) (12, 19), the relaxation can be on ultrafast (tens of femtoseconds) timescales. Experiments probing such dynamics require ultrafast (~20-fs) time resolution to capture these coupled electronic-vibrational dynamics. The time-resolved photoelectron spectroscopy technique has been widely used to monitor internal conversion through conical intersections (20–22), mainly for low-lying excited states. The nonradiative lifetimes can vary from several tens of femtoseconds, for internal conversion between low excited states of pyrazine (23) or pyrrole (24), for instance, to several hundreds of femtoseconds, which is the typical timescale for the nonradiative relaxation of polyatomic molecules to their ground state (25).

In this work, we implemented ultrafast VUV-driven photoelectron–photoion coincidence (PEPICO) imaging spectroscopy to investigate the highly excited neutral states of a model energetic molecule, methyl azide. Ultrafast (10-fs) high harmonic pulses at 8 eV were used to prepare a single highly excited state that is probed via multiphoton ionization by an IR laser field (Fig. 1). We found that when methyl azide is excited in the VUV at 8 eV, the vibrational wavepacket is nonadiabatically accelerated (i.e., accelerated faster than would adiabatically occur), leading to ultrafast internal conversion through a conical intersection to a dark state. This population transfer was complete on a surprisingly fast timescale of 25 fs, which is much faster than the adiabatic vibrational period of 135 fs for the most closely related vibrational mode, the CNN angle bend. These dynamics were directly evidenced by a very rapid increase in vibrational energy in the molecule, followed by a fast decrease in ionization signal induced by rapid population transfer to a dark state.

To uncover the mechanisms behind this ultrafast relaxation, we implemented a set of complementary advanced theoretical calculations to describe the excited states and resulting dynamics. These calculations showed that the initially prepared excited electronic state is mixed with both Rydberg and valence character. This excited electronic state strongly interacted with neighboring lower excited states through nonadiabatic couplings that drove large changes in the electronic and structural character of the molecule on an ultrafast timescale, ~10 fs. The wavepacket was quickly transferred to a lower excited state along one of the conical intersection seams, which led to a faster relaxation timescale than if the wavepacket had to travel all of the way to the MECI region. In fact, these nonadiabatic couplings were already strong in the Franck–Condon region, leading to a faster timescale for relaxation than is typical for the lowest excited state, when the time required for the wavepacket to reach a strong nonadiabatic region is typically longer (14, 26). These findings are important for understanding the unique strongly coupled non-Born–Oppenheimer molecular dynamics of highly excited states of neutral molecules.

Experimental Methods

For our experiments, we used an amplified Ti:Sapphire laser producing pulses at a wavelength of 780 nm with 1.5-mJ energy and 35-fs duration at a repetition rate of 10 kHz. Part of the laser output (200 μJ) was used to generate VUV pump pulses by focusing the beam into a xenon-filled hollow waveguide designed for high harmonic generation, producing odd harmonics of the driving frequency (5ω, 7ω) (27). To eliminate harmonics >7ω, we sent the beam through a 10-cm-long region filled with 3 torr of krypton. The fifth (8.0 eV) and seventh (11.2 eV) harmonics were then focused by using dielectric mirrors coated for 155 nm (Acton Optics), which were found to also reflect a useful amount of 7ω. The other part of the laser was attenuated to 20 μJ and used as a time-delayed probe pulse. The focused probe intensity was 9×10^{12} W/cm^2, well below the tunneling regime, but with sufficient intensity to drive two-photon processes. Harmonics were generated on the leading edge of the laser pulse, which also experienced self-phase modulation and blue-shifting due to ionization of the gas. Thus, they can shift in energy slightly during the high harmonic generation process (28, 29) and must be independently measured. In this work, the energy of 7ω was determined from the photoelectron spectra of known compounds (acetone and methyl azide), while 5ω was measured on a home-built spectrometer.

To measure electron and ion energies in coincidence, we used an imaging PEPICO spectrometer, shown schematically in Fig. 1, which has been described in detail (30). The detectors could measure the position and time-of-flight of the imaged ions and electrons. We recorded each ion–electron pair individually, keeping count rates low (0.1 counts per pulse average) to avoid false coincidences. Position and time-of-flight information allowed us to determine the full 3D momentum vector for each particle.

Optical choppers were placed in the path of each beam so that signal could be alternately collected with either the pump pulse or the probe pulse, or with both pulses present. In the limit of no dark current or signal saturation, the pump–probe signal is the signal with both pulses present minus the signal from each pulse by itself. The ionization potential of methyl azide (9.8 eV) is between harmonics 5ω and 7ω, so that only 7ω produces ions when the probe pulse is blocked (Figs. 1 and 3). When both pulses are present, 5ω creates a neutral excited state that is subsequently ionized by two photons from the probe pulse. An alternative signal pathway, where the IR probe interacts with a cation state prepared by 7ω, was ruled out by repeating the experiment with a thin film of glass (SiO_2; Lebow) placed in the pump beam path to remove 7ω and any higher harmonic. The involvement of more than two probe photons was ruled out by again repeating the experiment with a 390-nm probe (instead of 780 nm), with identical results aside from degraded time resolution.

Methyl azide was introduced into the ultrahigh vacuum chamber through an effusive nozzle with a backing pressure of 1 torr, approximately the vapor pressure of methyl azide held at −78 °C by an isopropanol/dry ice slurry (see *Methods* for synthesis and safe handling procedures of methyl azide).

Computational Methods

Accurate ab initio modeling of the full experiment—excitation, nonadiabatic evolution, photoionization, and subsequent dissociation of the cation—is computationally out of reach for any given level of theory. The strategy here was to combine several different levels of theory that could each tackle a part of the problem reliably, described briefly here and in more detail below. Geometry optimizations and single-point excited-state wavefunction calculations were carried out with the coupled-cluster (CC) methodology at a very high level of accuracy to identify the excited state accessed by the pump pulse. The mixed quantum-classical trajectory guided ab-initio multiple spawning (AIMS) method (31, 32) was then used to follow the dynamics of a wavepacket launched on this state and its relaxation to lower excited states. The photoionization probabilities were computed for all of the excited states involved in the dynamics to determine which excited states could be probed by the second pulse. Finally, the dissociation of the cation was modeled with the Gaussian suite of electronic structure programs (33). The complete basis set–atomic pair natural orbital (CBS-APNO) extrapolation method of Montgomery et al. (34) was used to compute accurate reaction barriers and bond energies. The CBS-APNO calculations have a mean absolute deviation of 0.5 kcal/mol (0.02 eV) for heats of reaction. By combining this complementary set of calculations, a full picture of both the structure and the dynamics for the full experiment could be pieced together.

CC calculations (35, 36) were performed with the PSI4 quantum chemistry program (37) to identify the nature of the excited state. Ground-state CC theory at the singles, doubles, and perturbative triples level CCSD(T) along with the aug-cc-pVTZ basis set (38, 39) was used to optimize an initial geometry. From this structure, equation-of-motion CCSD (EOM-CCSD) (40, 41) excited-state computations were undertaken. As no experimental absorption spectrum of methyl azide was available in the 8-eV energy range accessed by the pump pulse, the appropriate level of theory was chosen by also calculating the closely related HN_3, whose VUV absorption spectrum is known (*SI Appendix*). A doubly augmented, triple-zeta basis set (d-aug-cc-pVTZ) was necessary for adequate diffuseness of the basis set to properly describe the spatial extent of the system such that good agreement with experimental data for these highly excited states could be achieved. Such diffuse orbitals have been used with much success (42–44). By using this d-aug-cc-pVTZ basis set, states are accurate to within 0.1 eV.

The nonadiabatic dynamics following the photoexcitation by the pump pulse has been modeled by using the AIMS method, which describes simultaneously the electronic and nuclear dynamics and accounts for the nonadiabatic coupling between electronic states. In AIMS, the time-dependent wavefunction is expressed by a sum of products of a time-dependent nuclear wavefunction and an electronic wavefunction. For each electronic state, the time-dependent nuclear wavefunction is

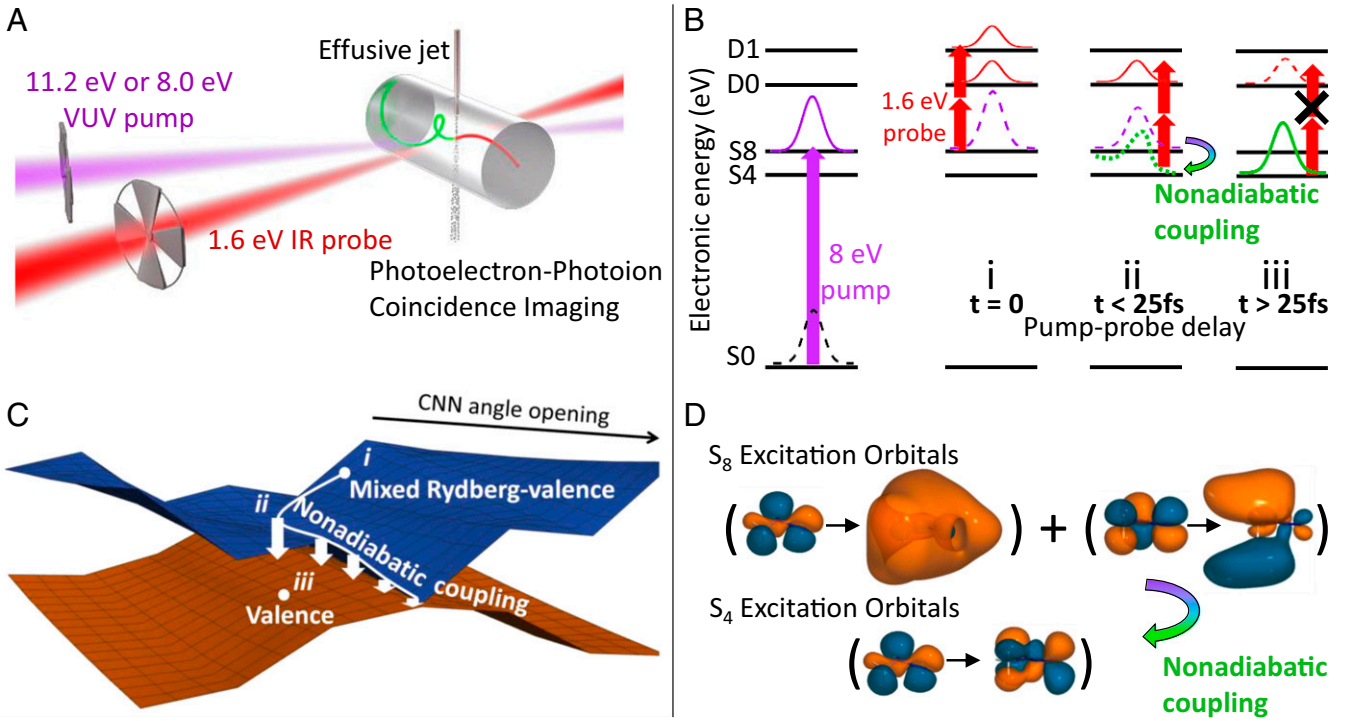

Fig. 1. Femtosecond PEPICO spectroscopy of methyl azide Rydberg–valence states. *A* shows two laser pulses which interact with an effusive molecular beam; the pump pulse prepares an excited state, which is then ionized by the probe pulse. Ionized fragments and their coincident electrons are detected with time- and position-sensitive detectors. *B* shows a schematic of the dynamics in the electronic states. The pump pulse excites a wavepacket on a highly excited state (S_8). If the second pulse probes the dynamics at time $t = 0$ (*B*, *i*), it ionizes the molecule to both the cation ground and first excited states. For pump–probe delay before 25 fs (*B*, *ii*), the wavepacket has time to evolve on the excited-state potential energy surface. Due to the corresponding increase in vibrational energy, the probe pulse can only ionize to the cation ground state. For longer pump–probe delays (*B*, *iii*), the wavepacket has completely relaxed to the dark S_4 state, due to strong nonadiabatic coupling, and the ion yield drops to zero. *C* shows a schematic representation of the potential energy surfaces of the mixed Rydberg–valence state accessed by the pulse and the dark valence state, as well as the conical intersection seam through which the population transfer occurs. The motion of the initial wavepacket on these surfaces is also shown with a white line, as well as points corresponding to the dynamics described in *B*. *D* shows excitation orbitals computed with EOM-CCSD for the initially prepared excited state, S_8, and the dark state, S_4. The initial S_8 state has mixed HOMO-excited and (HOMO-1) –excited character, with each component displaying mixed Rydberg and valence character. The dark S_4 state is a (HOMO-1) –excited valence state. Isocontours are 0.03 $|e|/Å^3$ for the mixed Rydberg–valence orbitals and 0.07 $|e|/Å^3$ for the pure valence orbitals.

expressed as a linear combination of trajectory basis functions, which are multidimensional frozen Gaussians whose positions and momenta are propagated classically following Hamilton's equations of motion. When a trajectory basis function enters in a region of strong nonadiabaticity (i.e., a region with a strong coupling between electronic and nuclear motion), a new basis function is spawned on the coupled electronic state, allowing for amplitude transfer. The amplitudes are obtained by solving the time-dependent Schrödinger equation in the basis of the trajectory basis functions. In AIMS, the potential energy surfaces and nonadiabatic couplings are computed on the fly at each time step. Additional information on the AIMS methodology can be found in the following reviews: refs. 32 and 45. For the simulations of methyl azide, we used AIMS as implemented in MOLPRO (46, 47), where the electronic structure and nonadiabatic couplings were computed at the state-average multiconfiguration self-consistent field (SA-MCSCF) level (*SI Appendix*). The dynamics were launched on the excited state accessed by the pump pulse for a swarm of 66 initial conditions sampled from a Wigner distribution of methyl azide's ground state. The simulations were run for 20 fs with a time step of 5 a.u., unless 80% or more of the population had been transferred to lower excited states.

The photoionization lifetimes—i.e., the time it takes to ionize 63% of the population under illumination by an electric field—were computed for the photoionization of all of the neutral excited states to the cationic ground state. The electronic structure of the neutral excited states and the cation was computed at the time-dependent density functional theory (TDDFT) level with the Coulomb-attenuating method (CAM) functional CAM-B3LYP (48) and the basis set 6–31+G(d) in Gaussian09 (33). The excitation energies and character of the excited states were in good agreement with the other electronic structure methods (*SI Appendix*). The lifetimes are inversely proportional to the square modulus of the photoionization coupling elements, which involved the computation of the dipole moment between the wavefunction of the ionized electron (described as a plane wave) and the Dyson orbitals (49, 50). The Dyson orbitals provide a correlated view of the orbital from which the electron has been ionized and play a crucial role in the interpretation of photoelectron lifetimes and angular distributions.

The Gaussian suite of programs (33) was used for the cation potential energy surface characterization. The geometries of the minima and the transition states were optimized by Hartree–Fock, hybrid density functional [B3LYP (51–53) and CAM-B3LYP (48)], second-order Møller–Plesset perturbation theory (54), and quadratic configuration interaction (55) methods. The spin-restricted vs. unrestricted stability of each structure was tested by using standard methods (56). The CBS-APNO extrapolation method of Montgomery et al. (34) was used to compute accurate energy differences. The CBS-APNO calculations have a mean absolute deviation of 0.5 kcal/mol (0.02 eV) for heats of reaction.

Results

Here, we first discuss our time-resolved experiments on the 8-eV excited state of methyl azide. To help interpret the time-resolved data, we then discuss single-photon ionization experiments conducted with the same total photon energy. For further insight, next, we turn to calculations. Separate calculations were performed to understand which excited state was excited by the pump pulse, how that excited state evolved nonadiabatically, how the probe pulse interacted with the wavepacket, and how the subsequent cation evolved and dissociated. The calculations allowed us to interpret our data to show that the electronic relaxation was driven by strong nonadiabatic coupling and that population transfer occurred along a seam well above the MECI.

VUV Pump–IR Probe of Methyl Azide Excited State Dynamics. We first discuss experiments where we used a VUV pump to prepare excited states of the neutral molecule, which were then probed by using a time-delayed IR pulse to ionize. Fig. 2 shows VUV pump–IR probe measurements using 5ω (8.0 eV) pump photons followed by a 2 × 1ω IR ionizing beam, which delivered a total of 11.2 eV to the system. The mass spectrum contained two signals: m/z = 57 amu, which is the methyl azide parent ion ($CH_3N_3^+$), and m/z = 28 amu, which is a fragment ion. At our combined photon energy (11.2 eV), the only energetically accessible, stable mass-28 ion was $HCNH^+$. Fig. 2*A* shows the time dependence of the two channels in the mass spectrum, revealing very fast dynamics. The molecular ion channel (green) appeared at $t = 0$ and decayed with a 21 ± 5-fs time constant. The fragment ion channel (red) rose with a 21-fs time constant and decayed with a 27 ± 5 fs time constant. This channel had an overall signal size ~7.5 times larger than the molecular ion channel. Overlaid on each signal is a fit curve shown as dashed black lines. As described in *SI Appendix*, each curve was fit with its decay time as the only adjustable parameter and was convolved with a Gaussian instrument response; the decay time found for the green curve was used as a fixed rise time for the red curve.

Having measured the ion transients, we next discuss the photoelectron spectra in coincidence with the parent ion. Pump–probe photoelectron spectra in coincidence with the parent ion are shown in Fig. 2*B*. These spectra show a single peak, starting at 1.01 eV at −40 fs and shifting linearly to 0.91 eV at +40 fs. By using the total photon energy (11.2 eV) minus the literature ionization energy (57) (9.8 eV) and the photoelectron kinetic energy (1.0 eV), the cation state reached by the probe must have 0.4 eV internal energy at early pump–probe delays and 0.5 eV at longer times. The lowest excited electronic state of the cation is 1.1 eV above the cation ground state (57), which ruled out electronic excitation. The observed 0.4–0.5 eV internal energy must then be vibrational energy.

Next, turning to the fragment ion, pump–probe photoelectron spectra in coincidence with the fragment ion channel are displayed in Fig. 2*C*. At early times, these spectra showed a broad feature at ~0.5 eV that corresponded to the vibrationally excited cation ground state and a spike at near-zero energies. The cation first excited electronic state, which has a vertical ionization potential of 11.4 eV and a Franck–Condon envelope that covers 10.9–11.9 eV, was a likely assignment for this spike at near-zero energies. The presence of ionization to both cation states suggested that the excited state has mixed character: Both the HOMO and the HOMO-1 electrons were involved in the excited state.

The fragment photoelectron data, too, showed a drift to lower electron kinetic energies, such that at long times (~75 fs), the spike near zero could not be observed anymore. This quasiballistic wavepacket moved into a region of the neutral excited state where we could not energetically access the cation excited state with our probe, but still had access to the cation ground state.

At first glance, the linear drop over time of the photoelectron kinetic energy would seem to have suggested that our signal decay may have been due to the wavepacket moving outside our spectral range (i.e., the energy gap between excited state and cation potential energy curves increasing to above our photon energy). However, the photoelectron energies were dropping at a rate of 1.2 meV/fs and would have taken 800 fs to drop from 1 eV to below threshold. Since the signal decay was much faster than that (25 fs), we concluded that signal decay was not due to the wavepacket motion on the excited state surface, but was due to some other process, such as internal conversion to a lower electronic state.

Single Photon Ionization of Methyl Azide. In pump–probe photoionization experiments, interpretation of the data relies heavily on knowledge of the final state populated after both pump and

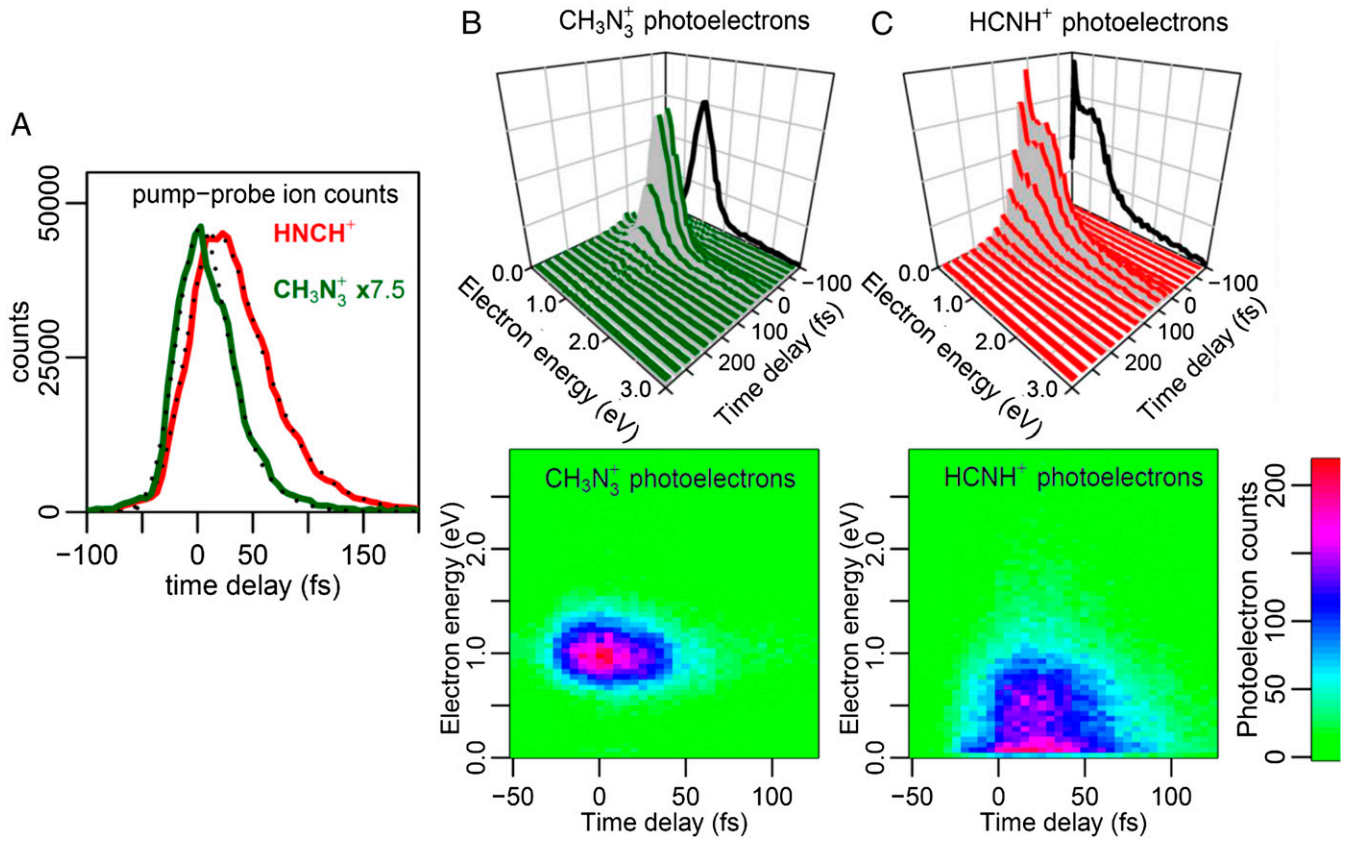

Fig. 2. VUV-excited state photoelectron–photoion counts show ultrafast 25-fs population transfer. *A* shows time-dependent ion yields for the 5ω-pump (8.0 eV), IR-probe (two photons of 1.6 eV each) measurements. The molecular ion decays in 21 fs, while the fragment ion shows a rise time of 21 fs and a decay time of 27 fs. *B* shows pump–probe photoelectron spectra recorded in coincidence with the molecular ion ($CH_3N_3^+$). The spectra are centered at 0.95 eV, indicating a ground-state cation with 0.45-eV vibrational energy. *C* shows pump–probe photoelectron spectra in coincidence with the fragment ion ($HCNH^+$). These spectra show a spike at 0 eV, indicating a contribution from the cation excited state, and a broad shoulder at 0.5 eV, indicating a contribution from highly vibrationally excited cation ground state.

probe pulses. Therefore, we turned to single-photon measurements to directly characterize the cation states. Here, we used 7ω (11.2 eV) to directly ionize the molecule and record the same PEPICO observables studied above. We observed the same mass spectrum (Fig. 3*B*): m/z = 57 amu ($CH_3N_3^+$) and m/z = 28 amu ($HCNH^+$).

Photoelectron spectra taken in coincidence with each mass signal are plotted in Fig. 3*C*. Electrons in coincidence with the mass 57 peak are shown in green with a binding energy of 9.9 eV (electron kinetic energy of 1.3 eV) and agree within 0.1 eV with the known vertical ionization potential of methyl azide (57). Electrons in coincidence with the fragment ion are shown in red and overlap those from the molecular ion but increase in amplitude all of the way to the photon threshold at 11.2 eV. The low binding energy part of this spectrum indicated that vibrationally excited levels of the ground electronic state of the cation have enough energy to cause dissociation, and the high binding energy part of the spectrum indicated that we also accessed the cation excited state. Literature photoelectron spectra show a vertical ionization potential of 11.4 eV for the cation excited state, but with a significant Franck–Condon width such that the low-energy edge of the cation excited state begins at ∼10.9 eV (57), easily accessible with our 11.2-eV photons. A breakdown diagram constructed from our data gives the appearance energy for the fragment at 10.2 eV, significantly lower than the prior literature value (10.5 eV) (58). The discrepancy was likely due to difficulties distinguishing counts originating from the effusive jet from those originating from the background.

The kinetic energy of the ion fragment is shown in Fig. 3*D*. The relatively large amount of translational energy, which peaked at 0.15 eV and extended up to ∼0.8 eV, explains the width of the m/z = 28 amu peak in the mass spectrum. This dissociation is slightly anisotropic (β = 0.15; Fig. 3 *D*, *Inset*). In dissociative ionization, a time constant cannot be directly inferred from the β-parameter as is done in neutral photodissociation (59); however, we could infer that the dissociation was comparable to or faster than molecular rotations.

As discussed above, the photoelectrons in coincidence with the m/z = 28 fragment indicated that the fragment could be formed from either a vibrationally excited cation ground state or from the cation excited state. Fragment translational energy curves were nearly identical in shape for the two cases, with a distribution peaking at 0.15 eV if the cation ground state was initially populated (shown in Fig. 3*D*) and 0.18 eV if the cation excited state was initially populated (*SI Appendix*). This suggests that either the two electronic states dissociate very similarly, which is possible but seems unlikely, or that the cation excited state internally converts to the cation ground state and then dissociates.

Comparing the single-photon data (Fig. 3) directly to the pump probe data (Fig. 2), we saw that the photoelectron spectra were qualitatively the same but shifted, and the ion kinetic energy release distributions were identical. These observations indicated that the dissociation events observed in the pump–probe experiment occurred in the cation manifold and that during the pump–probe time delay, the system remained as a bound methyl azide molecule. The ultrafast relaxation of the signal, then, was

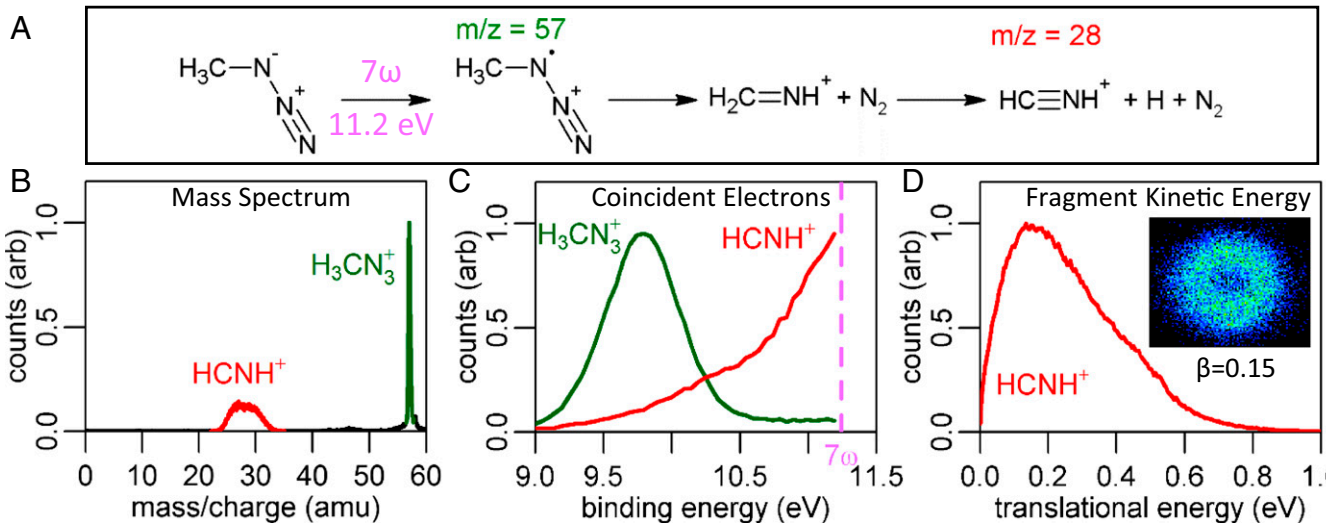

Fig. 3. Understanding the cation states of methyl azide. *A* illustrates the chemical pathway for dissociative ionization of CH_3N_3 determined by the one-photon data. The dissociation is a three-body, two-step breakup, with the first step involving a concerted rearrangement and dissociation to produce CH_2NH^+ and N_2. The CH_2NH^+ is produced with enough internal energy to subsequently break a CH bond to produce $HCNH^+$ and H. *B* shows the photoionization mass spectrum recorded after ionization by a single 7ω photon (11.2 eV). The molecular ion appears at $m/z = 57$, and a single fragmentation pathway is seen at $m/z = 28$; $HCNH^+$ is the only thermodynamically accessible and stable species for $m/z = 28$. *C* shows photoelectron spectra in coincidence with the molecular ion (green) and with the fragment ion (red). The literature vertical ionization potential is 9.8 eV. The fragment ions are dominantly coming from a cation excited state, but there is some contribution from a vibrationally excited cation ground state. *D* shows the kinetic energy of the fragment ion, which peaks at 0.15 eV and extends to ∼0.8 eV. The angular distribution of the fragments (*D*, *Inset*) are nearly isotropic, with an anisotropy parameter β equal to 0.15. arb, arbitrary units.

not due to the dissociation of the neutral, but rather to an internal conversion process to a lower electronic state.

Ab Initio Calculations of Neutral Excited State Character Populated by the VUV Pump Pulse. To identify the excited state populated by the pump pulse, we turned to high-accuracy CC calculations. The singlet excited states of methyl azide up to ∼8 eV include several valence and Rydberg states, including mixed states, which are built largely from the split π pair of the azide moiety (in methyl azide, the in-plane component of the azide π pair becomes a C–N σ bonding orbital, σ_{CN}, while the out-of-plane component remains a π nonbonding orbital, π^{nb}). Valence transitions from each of these orbitals to each of the split π* pair (into an in-plane σ* component and an out-of-plane π*) as well as transitions to low-*n* Rydberg states converging to each of the two lowest cation states occurr in the UV to VUV spectral range. The ground and first excited cation states are well described by a Koopmans' picture of the removal of an electron from π^{nb} and σ_{CN}, respectively [this picture breaks down in higher cation states, where hole mixing becomes important (60)].

The excited state populated at 8 eV was the eighth excited singlet state (labeled 3A′ or S_8) and was a mixture of two Rydberg states converging to different cation electronic states: π^{nb} (HOMO) → 3p and σ_{CN} (HOMO-1) → 3s (Fig. 1*D*), which converged to the cation ground and excited states, respectively. Each of these wavefunction components also displayed some valence character, with 3s being strongly mixed with σ* and 3p mixed with π*. This qualitative description of the wavefunction appeared at all levels of theory applied, including TD-DFT, MCSCF, and EOM-CC. The optimized geometries for the ground-state neutral, the S_8 excited state, and the two lowest cation states are given in Table 1. The only pronounced geometry change found in the excited state was in the CNN bond angle, which had an equilibrium value of 127°, somewhat intermediate between that of the π^{nb}- and σ_{CN}-hole cation states, due to the approximately equal contribution from each Rydberg state. The adiabatic potential energy minimum was 0.5 eV below the Franck–Condon region, agreeing with the experimentally observed amount of vibrational energy (Fig. 2 *B* and *C* compared with Fig. 3*C*). The mixing of the two Rydberg series led to dipole-allowed photoionization from the excited state to both cation states, as was seen in the pump–probe photoelectron data (Fig. 2*C*). However, the vibrational mode most closely matching the dominant geometry change had an excited-state vibrational frequency of 247.10 cm^{-1}, corresponding to a period of 135 fs, much slower than the observed dynamics.

The experimental measurements indicated that there was fast relaxation to a dark state for photoionization by our probe pulse. Below, we identify this state as S_4 (3A″); here, we describe the electronic character of this state and postpone a discussion of how we identify the state until *Dynamical Simulations of the Nonadiabatic Relaxation in the Neutral Excited State*. S_4 was composed of a single excitation σ_{CN} (HOMO-1) → π* and was of valence character (Fig. 1*D*). Due to its configuration, it had no dipole-allowed ionization to the cationic ground state (π^{nb}-hole), but had a dipole-allowed ionization to the lowest cationic excited state (σ_{CN}-hole). This made the S_4 state a dark state for our

Table 1. Important bond lengths and angles at the equilibrium geometries of the electronic states involved in pump–probe signal pathways

Geometric feature	S_0	S_8	D_0 (π^{-1})	D_1 (σ^{-1})
r(C—N1)/Å	1.484	1.499	1.477	1.483
r(N1—N2)/Å	1.250	1.256	1.327	1.207
r(N2—N3)/Å	1.145	1.139	1.126	1.157
∠CNN/°	113	127	113	151
∠NNN/°	174	178	169	174

S_0 was calculated at the CCSD(T)/aug-cc-pVTZ level; S_8 was EOM-CCSD/d-aug-cc-pVDZ level; and the radical cations were computed with CCSD/d-aug-cc-pVDZ. For the cation states, the orbital ionization occurred from is indicated in parentheses, with a −1 exponent to indicate an electron has been removed.

probe pulse, as 3.2 eV was not enough to ionize S_4 to the cation excited state; nonadiabatic population transfer to S_4 explained the decay of the ion signal. Between the S_4 and S_8 states, there were two Rydberg states (S_5/4A″ and S_7/5A″) composed of excitations from π^{nb} to in-plane 3p orbitals and one mixed state (S_6/2A′). The S_6 state had the same excitations as S_8, but was dominated by the π^{nb} (HOMO) → 3p component, unlike in S_8 where π^{nb} (HOMO) → 3p and σ_{CN} (HOMO-1) → 3s were more evenly mixed, with σ_{CN} (HOMO-1) → 3s slightly dominant.

Dynamical Simulations of the Nonadiabatic Relaxation in the Neutral Excited State. To supply additional evidence that internal conversion is the cause of the experimental signal decay, we turned to the calculation of nonadiabatic coupling vectors (NACs) and nonadiabatic wavepacket propagation. First, we focused on the NACs and gradient difference vectors at the equilibrium geometry of the neutral to assess which states were strongly coupled to the S_8 state accessed by the pump pulse. The electronic structure of the nine lowest electronic states and NACs were calculated at the SA9-MCSCF(4–8)/6–311+G(d) level by using an active space containing four electrons and eight orbitals: π, σ, π*, σ*, 3s, and a set of 3p orbitals (*SI Appendix*) and nine states in the state-averaging procedure (SA9). Large nonadiabatic coupling was found between the S_6 and S_8 states, which are both composed of similar Rydberg and valence excitations, as well as strong coupling from S_6 and S_8 to S_4, which originates from the $\sigma_{CN} \rightarrow 3s$ part of the S_6 and S_8 states. Since the S_4 state was dark for photoionization to the ground-state cation by the probe pulse, the relaxation to this state explained the experimental drop of ion yield as the pump–probe delay increased. No strong coupling was found between either S_6 or S_8 to the pure Rydberg state S_5. From these results, it seems likely that the S_8 excited state may relax by internal conversion to either S_6 or S_4, or potentially through S_6 then to S_4. However, no experimental signature was observed, within resolution, that clearly indicated the involvement of S_6, which was not a dark state with our probe pulse.

The timescale of the nonradiative relaxation, which is closely related the decay of the experimental signal, was determined from dynamical simulations carried out with the AIMS method. At the MCSCF(4–8)/6–311+G(d) level of theory used to compute the NACs above, we encountered severe convergence problems for the computation of these NACs between Rydberg states at geometries other than the equilibrium. To avoid this issue, we used a smaller active space without the 3p orbitals [SA6-CAS(4–5)/6–311+G(d)] and a smaller number of states (six instead of nine) in the state-averaging procedure (SA6), which removed states S_5 or S_7 entirely from the band and collapsed S_6 and S_8 into a single state of dominantly $\sigma_{CN} \rightarrow 3s + \sigma^*$ character. This new state was labeled S_{5SAS}, where the SAS subscript stands for small active space, and was taken to represent the S_8 state in the dynamical simulations. The other excited states (S_{1SAS} to S_{4SAS}) exhibited the same character as the S_1 to S_4 states in EOM-CC or MCSCF with the larger active space. At the ground-state equilibrium geometry, S_{5SAS} was found to be strongly coupled to S_{4SAS}, with very similar NAC vectors to those seen in the larger active space (see *SI Appendix* for further information). We took this to indicate that the forces acting on the wavepacket, at least in the Franck–Condon region, are determined largely by the $\sigma_{CN} \rightarrow 3s + \sigma^*$ component of the wavefunction and depend little on the (neglected) $\pi^{nb} \rightarrow 3p$ component; we thus proceeded with this reduced active space for the characterization of the conical intersection and the modeling of the nonadiabatic dynamics following the photoexcitation.

We identified a MECI between these two states with a peaked topology, emphasizing the funnel character of the population transfer (Fig. 4*C*). The geometry at the MECI had a large C–N1–N2 angle (141° rather than 113°) compared with the equilibrium geometry of MeN_3 ground state (Fig. 4*A*). The gradient difference vector followed, among others, the direction of the C–N1–N2 angle opening (Fig. 4*B*). This geometry variation was expected to occur during the excited state dynamics. The time-dependent mean value of the C–N1–N2 angle obtained from the nonadiabatic dynamical simulations is shown in Fig. 5*B*.

The dynamical simulations were carried out at the SA6-CAS (4–5)/6–311+G(d) level from the S_{5SAS} state ($\sigma_{CN} \rightarrow 3s + \sigma^*$ excitation, which is taken to represent the S_8 state of the larger active space) and corresponds to excited state accessed by the pump pulse. Due to the strong NACs already present in the Franck–Condon region, the electronic population transfer to the dark S_{4SAS} valence state was observed to occur on an ultrafast timescale much faster than the vibrational motion. In <20 fs, most of the population had been transferred to the dark state, which is in agreement with the measured drop of ion yield occurring on a similar timescale. As soon as the dynamics started, we observed a fast opening of the CNN bond angle up to ∼125° (Fig. 5*B*), near the adiabatic equilibrium geometry of the excited state. During this motion, the vibrational potential energy dropped by ∼0.6 eV (Fig. 5*A*), agreeing with both the (adiabatic) EOM-CC geometry optimization and the experimentally observed amount of vibrational energy (0.5 eV). However, the motion occurred in 10 fs, much faster than the adiabatically expected quarter-period of vibrational motion (135 fs /4 ∼ 34 fs). The ultrafast population transfer seen here did not proceed through the MECI itself (Fig. 4*C*), but rather along the seam (12–14) (Fig. 1*C* and *SI Appendix*). The MECI geometry had a CNN bond angle of 141°, but this angle only opened to ∼125° before the transfer of population to the dark state was essentially finished. We also calculated a decrease of the N1–N2 bond of 0.06 Å during the dynamics, shown in Fig. 5*B*. The close agreement between the calculated potential energy decrease and the experimental vibrational energy increase provided strong evidence that the calculation correctly describes where on the potential energy surface the population transfer occurs; in

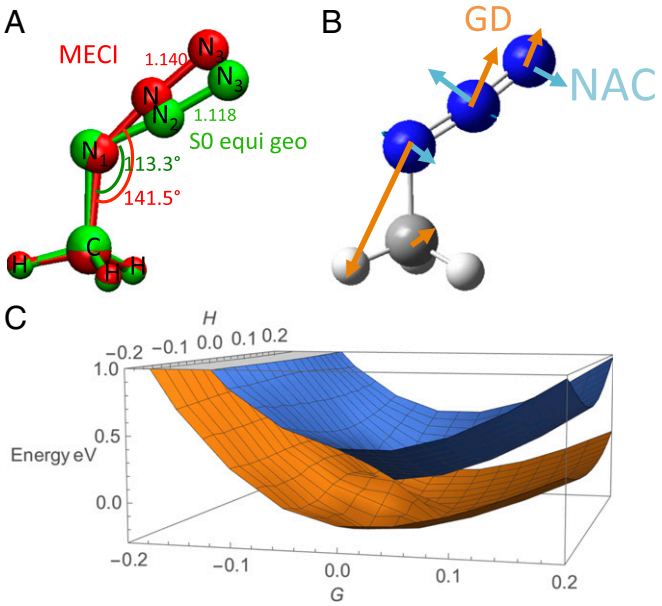

Fig. 4. (*A*) Comparison of the equilibrium geometry of MeN_3 ground state with the MECI S_{4SAS}/S_{5SAS} (which corresponds to S_4 and an effective state that represents S_8 in the larger active space). All of the electronic structure shown is computed at the SA6-CAS(4–5)/6–311+G(d) level. (*B*) NAC and gradient difference (GD) vectors at the geometry of the MECI. (*C*) S_{4SAS} and S_{5SAS} potential energy surfaces (in electronvolts) around the geometry of MECI as a function of the displacement along the nonadiabatic (*H*) and gradient difference vectors (*G*).

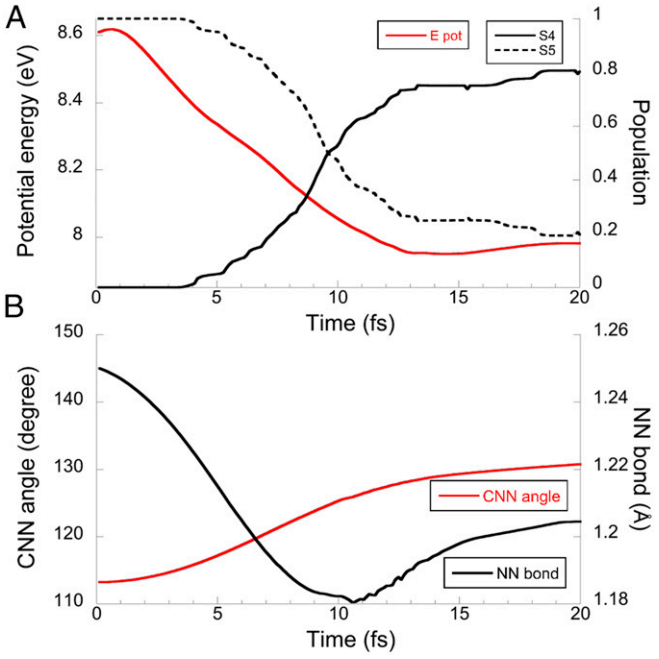

Fig. 5. (*A*) Population of the S_{4SAS} and S_{5SAS} electronic states during the nonadiabatic dynamics. The S_{5SAS} state of the reduced active space is taken to represent the S_8 state in the larger active space. The mean potential energy during the dynamics is also shown in red. (*B*) Variation of the CN1N2 angle and N1N2 bond distance in the first 20 fs of the nonadiabatic dynamics.

particular, the MECI was located 1.2 eV below the Franck–Condon region, and population transfer from this geometry would be accompanied by significantly more vibrational energy.

Ab Initio Calculations of the IR Photoionization of the Neutral Excited State by the Probe Pulse. The nonadiabatic dynamical simulations showed an ultrafast relaxation to the S_4 valence state. However, the experiment reports on the ion yield, so we computed the photoionization lifetimes of the neutral excited states to the cation ground state. The electronic structure was computed at the TD-DFT/CAM-B3LYP 6–31+G(d) level, which led to a good agreement of the character and energetics of the excited states with EOM-CCSD/d-aug-cc-pVDZ results (*SI Appendix*, Table S2). The photoionization lifetimes require the computation of the Dyson orbitals that represent the orbital from which the electron is ionized (49). Since the cation ground state was well described in the Koopmans' picture by the removal of the π^{nb} electron, the Dyson orbital of an electronic state reflects the excitation(s) from the π^{nb} orbital.

At the equilibrium geometry of the ground state, the mixed valence–Rydberg and pure Rydberg states (S_5 to S_8) had very short photoionization lifetimes (between 2 and 25 fs) due to their diffuse Rydberg orbital (50), which indicated that they should promptly ionize during the probe pulse. On the other hand, the S_4 valence state exhibited a very long lifetime (>4 ps) because it had no excitation from the π^{nb} orbital, so it would not be significantly ionized by the probe pulse. As the probe pulse also ionizes the wavepacket when it leaves the FC region, we investigated the effect of geometrical changes on the photoionization lifetimes. For the S_4 and the pure Rydberg states (S_5 and S_7), the lifetimes remained similar as we approached the MECI geometry. The behavior was different for the two mixed valence–Rydberg states S_6 and S_8. The highest state (S_8), which is optically accessed by the pulse, lost its valence character, which did not significantly impact its photoionization lifetime. The other mixed valence–Rydberg state (S_6) lost its Rydberg character when approaching the MECI geometry, so its ionization lifetime increased by several orders of magnitude, which may explain the lack of clear experimental evidence for the involvement of S_6. (More information on the photoionization is available in *SI Appendix*.)

Ab Initio Calculations of Cation States and Dissociation After the IR Probe Pulse. In PEPICO spectroscopy, a measurement does not end until the ion hits its detector, tens of microseconds after the pump and probe pulses. To interpret these asymptotic processes in the cation, we turned to ab initio calculations of the cation ground-state potential energy surface, at the CBS-APNO level. These calculations indicated that only one dissociation pathway was energetically accessible, a two-step, three-body breakup with a barrier of 10.49 eV. In this pathway, a hydrogen atom migrated from the methyl group to the adjacent nitrogen atom as the N1–N2 bond broke; there was a concerted rearrangement and bond breaking to form the methylenimine cation ($CH_2 = NH^+$ m/z 29) and a neutral nitrogen molecule (N_2).

Although the dissociative ionization of methyl azide initially formed $CH_2{=}NH^+$, no mass 29 signal was observed. This indicated that the methylenimine cation intermediate was formed with an internal energy sufficient to cause further fragmentation on a submicrosecond timescale; the barrier for breaking the CH bond in methylenimine cation is 1.35 eV (61), providing us with an estimate for the minimum internal energy of the methylenimine cation intermediate.

Our ab initio calculations showed that the barrier to dissociation on the cation excited state is ∼2.0 eV, which was not energetically accessible with our 11.2-eV photons, and the fragmentation must occur after internal conversion to the cation ground state. The result that the dissociation must occur on the cation ground state explained the similarity between ion fragment kinetic energy distributions recorded in coincidence with electrons from cation ground and excited states.

Discussion

In this experiment, a high-energy-density molecule, methyl azide, was promoted into a highly excited neutral state, where there was a dense manifold of electronic states strongly coupled to one another. Experimentally, ionization counts from this excited-state decay within a very fast timescale of 25 fs. Our ab initio calculations showed that the absorbing state at 8 eV had both Rydberg–Rydberg and Rydberg–valence mixing, and the wavepacket moved quickly toward a strong nonadiabatic coupling region. Our wavepacket propagation calculations showed that the motion was dominated by a large-amplitude opening of the CNN bond angle, from 113° to 125° (Fig. 5), that approached a conical intersection seam within 10 fs, thus explaining our experimental observation of a 25-fs excited-state decay. This motion was approximately a quarter-cycle of the corresponding excited-state adiabatic harmonic vibrational mode and would take 34 fs if the wavepacket evolved adiabatically; that the motion occurs in 25 fs indicated that the Born–Oppenheimer approximation fails at a quantitative level to describe even the initial dynamics of the system. Interestingly, the electronic population transfer occurred in 25 fs, despite the fact that the seam of conical intersections was outside the Franck–Condon region.

As the wavepacket was accelerated on the initially excited potential energy surface, the experimentally detected mass spectrum shifted from the parent ion ($CH_3N_3^+$) to the fragment ion ($HNCH^+$), as a consequence of the extra vibrational energy in the ion. The actual dissociation event occurred well after the probe pulse, but long before the ion finished traveling down the flight tube of the ion detector.

Note that lower excited states of many organic azides, which correspond to the states populated after the nonadiabatic

dynamics observed here, generally have lifetimes of a few hundred femtoseconds (62–64), while the lowest excited state has a lifetime of a few to several hundred picoseconds (65–67). The asymptotic (longtime) products formed from VUV excitation of methyl azide, which occurred after the short-timescale nonadiabatic dynamics discussed here, have been explored in detail by Wodtke and coworkers (68–71), including minor pathways for ion-pair formation (71) and cyclic N_3 formation (70). Indeed, very recently, detailed measurements became available of the neutral dissociation products formed after excitation at 157 nm, very close to our pump wavelength (72). The initial dissociation is dominated by N1–N2 bond cleavage to form N_2 and CH_3N and a C–N1 bond cleavage to form CH_3 and cyclic N_3. Both channels produce fragments that continue on to secondary dissociation events.

The behavior expected from an adiabatic point of view can be inferred from the EOM-CC calculations. The excited state produced in the Franck–Condon region at 8 eV in methyl azide was an almost equal mixture of two Rydberg–valence components, π^{nb} (HOMO) → 3p + π^* and σ_{CN} (HOMO-1) → 3s + σ^*. The equilibrium structure of this state approximately averaged the two lowest-energy cation structures, giving an equilibrium CNN bond angle of 127° and an N1–N2 bond length of 1.26 Å and indicating that the Rydberg components dominated the adiabatic behavior. Purely adiabatic dynamics, then, can explain the opening of the bond angle, but not the fast rate of the dynamics. These observations emphasize that purely adiabatic arguments are inadequate, and nonadiabatic calculations must be used to model the experiment.

More generally, the fast population transfer seen here may represent a nearly universal response to small molecules excited by VUV pulses in the 7- to 9-eV energy range. The adiabatic S_8 state included a mixing between two diabatic Rydberg states (π^{nb} → 3p and σ_{CN} → 3s) and a diabatic valence state (σ_{CN} → σ^*). The excited state here was an almost 50/50 mix of HOMO-excited and (HOMO-1) –excited character, indicating that we were approaching the strong-coupling limit (i.e., the coupling was large compared with the energy difference between basis states). Although apparently coincidental, a near-degeneracy between low-n Rydberg states of different series may actually be quite common. Using typical quantum defects [$\delta \sim 1$ for an s-wave and $\delta \sim 0.5$ for a p-wave (73, 74)], we would expect HOMO → 3p and (HOMO-1) → 3s to be within a few tenths of an electronvolt anytime the first two ionization potentials are separated by ∼1.2 eV, which is a reasonably common situation for organic molecules (75). Considering the number of potential Rydberg–Rydberg interactions that may occur (i.e., near-degenerate pairs other than HOMO → 3p and HOMO-1 → 3s), it seems likely that near-degeneracies between low-n Rydberg states may be ubiquitous in the 7- to 9-eV energy range in organic molecules.

Another important aspect of the electronic mixing seen in methyl azide is that the two components of the wavefunction differ by two electrons, which affects experimental observables such as the photoelectron angular distribution (PAD). The large majority of femtosecond PAD measurements have studied conical intersections between S_1 and S_2 states (20, 76), which are usually (but not always) HOMO → LUMO and HOMO → (LUMO + 1). The excited-state wavefunction in these cases can be written as $|\phi_a^{-1}\phi_c^1\rangle + |\phi_a^{-1}\phi_d^1\rangle = |\phi_a^{-1}\rangle(|\phi_c^1\rangle + |\phi_d^1\rangle)$, where a "−1" superscript indicates a hole in a usually filled orbital and a "1" superscript indicates an electron in a usually empty orbital. If the wavefunction can be written this way, the two parts $(|\phi_c^1\rangle + |\phi_d^1\rangle)$ interfere, and the PAD becomes a sensitive measurement of electronic changes. Antisymmetrization of the electronic wavefunction does not change this result. However, in the case of methyl azide, the wavefunction is of the form $|\phi_a^{-1}\phi_c^1\rangle + |\phi_b^{-1}\phi_d^1\rangle$, sometimes referred to as "nonconjugate" mixing (74), which causes the PADs from ϕ_c^1 and ϕ_d^1 to add as probability densities rather than as amplitudes. This makes the total PAD much less sensitive as an indicator of electronic changes, despite the fact that such a system would normally be considered a case of "corresponding" continua (77, 78). In light of the potentially near-ubiquitous nature of electronic Rydberg–Rydberg mixing and the two-electron differences such mixing creates, the additional information available in PEPICO has advantages over PAD measurements.

Conclusions

Highly excited neutral states near 8 eV of a model energetic molecule, methyl azide, were investigated by femtosecond VUV-pump, IR-probe coincidence spectroscopy and modeled in detail with CBS-APNO, EOM-CC, and MCSCF calculations. The initially prepared excited state displayed both electronic Rydberg–Rydberg mixing and Rydberg–valence mixing. It underwent rapid, but specific, nonadiabatic relaxation to a lower-lying valence state on a 25-fs timescale, providing direct experimental observations of the nonadiabatic relaxation of highly excited states with femtosecond resolution. Moreover, these phenomena may be reasonably ubiquitous in the 7- to 9-eV energy range for organic molecules.

Methods

Methyl azide was prepared by established procedures (68, 79), slightly modified to increase safety. It should be noted that although methyl azide is an explosive molecule, the large majority of reported accidents have been traced to either hydrazoic acid or heavy metal azide formation (80). Consequently, the procedure here used clean glassware that had never been used with heavy metal salts, and the use of protic solvents was avoided. Sodium azide was dissolved in DMSO and warmed to 80 °C under flowing helium. An equimolar amount of dimethyl sulfate was slowly injected, causing the reaction mixture to bubble. The gas flow was passed over KOH pellets to remove both any moisture and any hydrazoic acid, then through a liquid nitrogen cold finger, where the methyl azide collected as a bright white powder. Mass spectra of the sample indicated that the product was methyl azide (*m/z* 57) with a small amount of dimethyl ether (*m/z* 46); the dimethyl ether could be removed by warming the sample to −78 °C on a dry ice isopropanol slurry and pumping overnight. Because methyl azide is shock sensitive, it is recommended to avoid using more than ∼10 mg at a time.

ACKNOWLEDGMENTS. This work was supported by Department of Energy Office of Basic Energy Sciences Grant DE-SC0012628. D.E.C. and Q.L.N. were supported by the National Science Foundation Graduate Research Program Grants DGE-1650115 and DGE-1144083. B.M. and F.R. were supported by the Fonds National de la Recherche Scientifique (FNRS), Belgium; and the Consortium des Equipements de Calcul Intensif for Computational Resources Grant FNRS 2.5020.11. R.C.F. was supported by Georgia Southern University start-up funds and by NASA Grant NNX17AH15G.

1. Marsh DR (2011) Chemical–Dynamical coupling in the mesosphere and lower thermosphere. *Aeronomy of the Earth's Atmosphere and Ionosphere*, eds Abdu MA, Pancheva D (Springer, Dordrecht, The Netherlands), pp 3–17.
2. Lühr H, Liu H, Park J, Müller S (2011) New aspects of the coupling between thermosphere and ionosphere, with special regards to CHAMP mission results. *Aeronomy of the Earth's Atmosphere and Ionosphere*, eds Abdu MA, Pancheva D (Springer, Dordrecht, The Netherlands), pp 303–316.
3. Öberg KI (2016) Photochemistry and astrochemistry: Photochemical pathways to interstellar complex organic molecules. *Chem Rev* 116:9631–9663.
4. Böhme DK (2011) Multiply-charged ions and interstellar chemistry. *Phys Chem Chem Phys* 13:18253–18263.
5. Bhattacharya A, Guo Y, Bernstein ER (2010) Nonadiabatic reaction of energetic molecules. *Acc Chem Res* 43:1476–1485.
6. Bernsein ER (2005) Role of excited electronic states in the decomposition of energetic materials. *Overviews of Recent Research on Energetic Materials*, Advanced Series in Physical Chemistry, eds Shaw RW, Brill TB, Thompson DL (World Scientific Publishing, Singapore), pp 161–189.
7. Dlott DD (2003) Fast molecular processes in energetic materials. *Energetic Materials Part 2. Detonation, Combustion, Theoretical and Computational Chemistry*, eds Politzer P, Murray J (Elsevier, Amsterdam), pp 125–191.
8. Kuklja MM (2003) On the initiation of chemical reactions by electronic excitations in molecular solids. *Appl Phys A Mater Sci Process* 76:359–366.

9. Berkowitz J (1979) *Photoabsorption, Photoionization, and Photoelectron Spectroscopy* (Academic, New York).
10. Domcke W, Yarkony D, Köppel H, eds (2011) *Conical Intersections: Theory, Computation and Experiment* (World Scientific, Singapore).
11. Klessinger M, Michl J (1995) *Excited States and Photochemistry of Organic Molecules* (VCH, New York).
12. Levine BG, Martínez TJ (2007) Isomerization through conical intersections. *Annu Rev Phys Chem* 58:613–634.
13. Boggio-Pasqua M, Ravaglia M, Bearpark MJ, Garavelli M, Robb MA (2003) Can diarylethene photochromism be explained by a reaction path alone? A CASSCF study with model MMVB dynamics. *J Phys Chem A* 107:11139–11152.
14. Mignolet B, Curchod BFE, Martínez TJ (2016) Rich athermal ground-state chemistry triggered by dynamics through a conical intersection. *Angew Chem Int Ed Engl* 55: 14993–14996.
15. Kasha M (1950) Characterization of electronic transitions in complex molecules. *Discuss Faraday Soc* 9:14–19.
16. Mahapatra S (2009) Excited electronic states and nonadiabatic effects in contemporary chemical dynamics. *Acc Chem Res* 42:1004–1015.
17. Matsika S, Krause P (2011) Nonadiabatic events and conical intersections. *Annu Rev Phys Chem* 62:621–643.
18. Bernstein ER (2014) On the release of stored energy from energetic materials. *Adv Quantum Chem* 69:31–69.
19. Domcke W, Yarkony DR (2012) Role of conical intersections in molecular spectroscopy and photoinduced chemical dynamics. *Annu Rev Phys Chem* 63:325–352.
20. Stolow A, Bragg AE, Neumark DM (2004) Femtosecond time-resolved photoelectron spectroscopy. *Chem Rev* 104:1719–1758.
21. Blanchet V, Zgierski MZ, Seideman T, Stolow A (1999) Discerning vibronic molecular dynamics using time-resolved photoelectron spectroscopy. *Nature* 401:52–54.
22. Hockett P, Bisgaard CZ, Clarkin OJ, Stolow A (2011) Time-resolved imaging of purely valence-electron dynamics during a chemical reaction. *Nat Phys* 7:612–615.
23. Suzuki Y, Fuji T, Horio T, Suzuki T (2010) Time-resolved photoelectron imaging of ultrafast S2→S1 internal conversion through conical intersection in pyrazine. *J Chem Phys* 132:174302.
24. Wu G, et al. (2015) Excited state non-adiabatic dynamics of pyrrole: A time-resolved photoelectron spectroscopy and quantum dynamics study. *J Chem Phys* 142:074302.
25. Ullrich S, Schultz T, Zgierski MZ, Stolow A (2004) Direct observation of electronic relaxation dynamics in adenine via time-resolved photoelectron spectroscopy. *J Am Chem Soc* 126:2262–2263.
26. Polli D, et al. (2010) Conical intersection dynamics of the primary photoisomerization event in vision. *Nature* 467:440–443.
27. Durfee CG, et al. (1999) Phase matching of high-order harmonics in hollow waveguides. *Phys Rev Lett* 83:2187–2190.
28. Shin HJ, et al. (2001) Nonadiabatic blueshift of high-order harmonics from Ar and Ne atoms in an intense femtosecond laser field. *Phys Rev A* 63:053407.
29. Froud CA, et al. (2006) Soft-x-ray wavelength shift induced by ionization effects in a capillary. *Opt Lett* 31:374–376.
30. Gagnon E, et al. (2008) Time-resolved momentum imaging system for molecular dynamics studies using a tabletop ultrafast extreme-ultraviolet light source. *Rev Sci Instrum* 79:063102.
31. Martinez TJ, Ben-Nun M, Levine RD (1996) Multi-electronic-state molecular dynamics: A wave function approach with applications. *J Phys Chem* 100:7884–7895.
32. Ben-Nun M, Martínez TJ (2002) Ab initio quantum molecular dynamics. *Advances in Chemical Physics*, eds Prigogine I, Rice SA (John Wiley & Sons, Inc., New York), Vol 121, pp 439–512.
33. Frisch MJ, et al. (2013) Gaussian09 (Gaussian, Inc., Wallingford, CT), Version D.01.
34. Montgomery JA, Ochterski JW, Petersson GA (1994) A complete basis set model chemistry. IV. An improved atomic pair natural orbital method. *J Chem Phys* 101: 5900–5909.
35. Crawford TD, Schaefer HF (2000) An introduction to coupled cluster theory for computational chemists. *Reviews in Computational Chemistry*, eds Lipkowitz KB, Boyd DB (John Wiley & Sons, Inc., Hoboken, NJ), Vol 14, pp 33–136.
36. Shavitt I, Bartlett RJ (2009) *Many-Body Methods in Chemistry and Physics: MBPT and Coupled-Cluster Theory* (Cambridge Univ Press, Cambridge, UK).
37. Turney JM, et al. (2012) Psi4: An open-source *ab initio* electronic structure program. *Wiley Interdiscip Rev Comput Mol Sci* 2:556–565.
38. Raghavachari K, Trucks GW, Pople JA, Head-Gordon M (1989) A fifth-order perturbation comparison of electron correlation theories. *Chem Phys Lett* 157:479–483.
39. Dunning TH (1989) Gaussian basis sets for use in correlated molecular calculations. I. The atoms boron through neon and hydrogen. *J Chem Phys* 90:1007–1023.
40. Stanton JF, Bartlett RJ (1993) The equation of motion coupled-cluster method. A systematic biorthogonal approach to molecular excitation energies, transition probabilities, and excited state properties. *J Chem Phys* 98:7029–7039.
41. Krylov AI (2008) Equation-of-motion coupled-cluster methods for open-shell and electronically excited species: The hitchhiker's guide to fock space. *Annu Rev Phys Chem* 59:433–462.
42. Fortenberry RC, King RA, Stanton JF, Crawford TD (2010) A benchmark study of the vertical electronic spectra of the linear chain radicals C(2)H and C(4)H. *J Chem Phys* 132:144303.
43. Morgan WJ, Fortenberry RC (2015) Additional diffuse functions in basis sets for dipole-bound excited states of anions. *Theor Chem Acc* 134:47.
44. Theis ML, Candian A, Tielens AGGM, Lee TJ, Fortenberry RC (2015) Electronically excited states of PANH anions. *Phys Chem Chem Phys* 17:14761–14772.
45. Martínez TJ (2006) Insights for light-driven molecular devices from *ab initio* multiple spawning excited-state dynamics of organic and biological chromophores. *Acc Chem Res* 39:119–126.
46. Werner H-J, Knowles PJ, Knizia G, Manby FR, Schütz M (2012) Molpro: A general-purpose quantum chemistry program package. *Wiley Interdiscip Rev Comput Mol Sci* 2:242–253.
47. Levine BG, Coe JD, Virshup AM, Martínez TJ (2008) Implementation of ab initio multiple spawning in the Molpro quantum chemistry package. *Chem Phys* 347:3–16.
48. Yanai T, Tew DP, Handy NC (2004) A new hybrid exchange–Correlation functional using the Coulomb-attenuating method (CAM-B3LYP). *Chem Phys Lett* 393:51–57.
49. Oana CM, Krylov AI (2007) Dyson orbitals for ionization from the ground and electronically excited states within equation-of-motion coupled-cluster formalism: Theory, implementation, and examples. *J Chem Phys* 127:234106.
50. Mignolet B, Johansson JO, Campbell EEB, Remacle F (2013) Probing rapidly-ionizing super-atom molecular orbitals in C_{60}: A computational and femtosecond photoelectron spectroscopy study. *ChemPhysChem* 14:3332–3340.
51. Becke AD (1993) A new mixing of Hartree–Fock and local density-functional theories. *J Chem Phys* 98:1372–1377.
52. Becke AD (1993) Density-functional thermochemistry. III. The role of exact exchange. *J Chem Phys* 98:5648–5652.
53. Lee C, Yang W, Parr RG (1988) Development of the Colle-Salvetti correlation-energy formula into a functional of the electron density. *Phys Rev B Condens Matter* 37:785–789.
54. Møller C, Plesset MS (1934) Note on an approximation treatment for many-electron systems. *Phys Rev* 46:618–622.
55. Pople JA, Head-Gordon M, Raghavachari K (1987) Quadratic configuration interaction. A general technique for determining electron correlation energies. *J Chem Phys* 87:5968–5975.
56. Seeger R, Pople JA (1977) Self-consistent molecular orbital methods. XVIII. Constraints and stability in Hartree–Fock theory. *J Chem Phys* 66:3045–3050.
57. Cradock S, Ebsworth EAV, Murdoch JD (1972) Photoelectron spectra of some group 4 pseudohalides and related compounds. *J Chem Soc, Faraday Trans II* 68:86–100.
58. Franklin JL, Dibeler VH, Reese RM, Krauss M (1958) Ionization and dissociation of hydrazoic acid and methyl azide by electron impact. *J Am Chem Soc* 80:298–302.
59. Li W, et al. (2003) Dissociative photoionization dynamics in ethane studied by velocity map imaging. *Chem Phys Lett* 374:334–340.
60. von Niessen W, Tomasello P (1989) Many-body effects in the ionization spectra of azides. *J Electron Spectrosc Relat Phenom* 48:187–201.
61. Zhou J, Schlegel HB (2009) Ab initio classical trajectory study of the dissociation of neutral and positively charged methanimine (CH_2NH^{n+} n = 0-2). *J Phys Chem A* 113: 9958–9964.
62. Burdzinski G, et al. (2006) Early events in the photochemistry of aryl azides from femtosecond UV/Vis spectroscopy and quantum chemical calculations. *J Am Chem Soc* 128:13402–13411.
63. Kubicki J, et al. (2009) Direct observation of acyl azide excited states and their decay processes by ultrafast time resolved infrared spectroscopy. *J Am Chem Soc* 131: 4212–4213.
64. Wang J, et al. (2007) Early events in the photochemistry of 2-naphthyl azide from femtosecond UV/Vis spectroscopy and quantum chemical calculations: Direct observation of a very short-lived singlet nitrene. *J Org Chem* 72:7581–7586.
65. Kuzmin AV, Neumann C, van Wilderen LJGW, Shainyan BA, Bredenbeck J (2016) Exploring photochemistry of p-bromophenylsulfonyl, p-tolylsulfonyl and methylsulfonyl azides by ultrafast UV-pump-IR-probe spectroscopy and computations. *Phys Chem Chem Phys* 18:8662–8672.
66. Kubicki J, et al. (2011) Photochemistry of 2-naphthoyl azide. An ultrafast time-resolved UV-vis and IR spectroscopic and computational study. *J Am Chem Soc* 133: 9751–9761.
67. Vyas S, et al. (2012) An ultrafast time-resolved infrared and UV-vis spectroscopic and computational study of the photochemistry of acyl azides. *J Phys Org Chem* 25:693–703.
68. Quinto-Hernandez A, Wodtke AM, Bennett CJ, Kim YS, Kaiser RI (2011) On the interaction of methyl azide (CH_3N_3) ices with ionizing radiation: Formation of methanimine (CH_2NH), hydrogen cyanide (HCN), and hydrogen isocyanide (HNC). *J Phys Chem A* 115:250–264.
69. Larson C, et al. (2006) Collision-free photochemistry of methylazide: Observation of unimolecular decomposition of singlet methylnitrene. *J Chem Phys* 125:133302.
70. Quinto-Hernandez A, et al. (2012) Photofragmentation translational spectroscopy of methyl azide (CH_3N_3) photolysis at 193 nm: Molecular and radical channel product branching ratio. *J Phys Chem A* 116:4695–4704.
71. Quinto-Hernandez A, et al. (2011) Photoionization of CH_3N_3 produces $^3B_2N_3^-$: A theoretical and experimental study of the ion-pair channel. *J Phys Chem Lett* 2: 2311–2315.
72. Quinto-Hernandez A, Lee S-H, Wodtke AM (2017) The collision-free photochemistry of methyl azide at 157 nm: Mechanism and energy release. *J Chem Phys* 147:064307.
73. Reisler H, Krylov AI (2009) Interacting Rydberg and valence states in radicals and molecules: Experimental and theoretical studies. *Int Rev Phys Chem* 28:267–308.
74. Robin MB (1974) *Higher Excited States of Polyatomic Molecules* (Academic, New York).
75. Turner DW (1970) *Molecular Photoelectron Spectroscopy: A Handbook of He 584 Å Spectra* (Wiley Interscience, London).
76. Suzuki T (2014) Ultrafast electronic dynamics in polyatomic molecules studied using femtosecond vacuum ultraviolet and x-ray pulses. *J Phys B At Mol Opt Phys* 47:124001.
77. Pratt ST (2004) Photoionization of excited states of molecules. *Radiat Phys Chem* 70: 435–452.
78. Wu G, Hockett P, Stolow A (2011) Time-resolved photoelectron spectroscopy: From wavepackets to observables. *Phys Chem Chem Phys* 13:18447–18467.
79. Teslja A, Nizamov B, Dagdigian PJ (2004) The electronic spectrum of methyleneimine. *J Phys Chem A* 108:4433–4439.
80. Martel B (2000) *Chemical Risk Analysis: A Practical Handbook* (Taylor & Francis, New York).